Efficient Nonthermal Ion and Electron Acceleration Enabled by the Flux-Rope Kink Instability in 3D Nonrelativistic Magnetic Reconnection

Qile Zhang [*], Fan Guo, William Daughton, and Hui Li
Los Alamos National Laboratory, Los Alamos, New Mexico 87545, USA

Xiaocan Li
Dartmouth College, Hanover, New Hampshire 03755, USA

The relaxation of field-line tension during magnetic reconnection gives rise to a universal Fermi acceleration process involving the curvature drift of particles. However, the efficiency of this mechanism is limited by the trapping of energetic particles within flux ropes. Using 3D fully kinetic simulations, we demonstrate that the flux-rope kink instability leads to strong field-line chaos in weak-guide-field regimes where the Fermi mechanism is most efficient, thus allowing particles to transport out of flux ropes and undergo further acceleration. As a consequence, both ions and electrons develop clear power-law energy spectra that contain a significant fraction of the released energy. The low-energy bounds are determined by the injection physics, while the high-energy cutoffs are limited only by the system size. These results have strong relevance to observations of nonthermal particle acceleration in space and astrophysics.

Introduction.—Within space and astrophysical plasmas, magnetic fields often develop stressed current sheets that are susceptible to magnetic reconnection—a process that rapidly reconfigures the magnetic topology leading to high-speed flows, plasma heating, and nonthermal particle acceleration [1]. Understanding this acceleration physics has immediate applications to the magnetosphere, solar flares, and various astrophysical problems. Observations from both the solar corona [2–5] and magnetotail [6,7] show simultaneous productions of ion and electron power-law energy distributions extending to high energy during reconnection, suggesting a common physical origin. However, the underlying physics remains poorly understood, since researchers have previously failed to produce these power laws within self-consistent kinetic simulations in the relevant regime.

On the theoretical front, previous studies have demonstrated a Fermi-type mechanism within reconnection layers [8–13], involving the particle curvature drift within the electric field induced by the large-scale flows. This mechanism, driven by field-line curvature, is efficient for low guide field (out of the reconnection plane) to reconnection field ratios $b_g < 0.5$ [11–14] and is enhanced by magnetic-island interactions within the reconnection layer. However, in 2D simulations, the efficiency of the Fermi acceleration is limited by particle trapping within these islands. Several 3D studies have demonstrated that overlapping tearing islands due to multiple resonance surfaces lead to field-line chaos [15–18], allowing energetic particles to transport out of flux ropes and continue acceleration [10,13,19]. However, this mechanism only applies to regimes with

significant guide fields ($b_g > 0.5$) where the efficiency of the Fermi mechanism is dramatically reduced.

With 3D kinetic simulations, here we demonstrate that, within the weak-guide-field regime, the flux-rope kink instability is unstable in the reconnection layer. This generates strong field-line chaos, allowing energetic particles to transport out of flux ropes and continue Fermi acceleration. The field-line chaos is triggered when flux ropes reach a threshold length for the $m = 1$ kink instability. Our 3D simulations exploiting this threshold reach an unprecedented domain size. For the first time, both protons and electrons develop clear and sustainable nonthermal power laws. The nonthermal populations contain a significant fraction of the released energy, and nonthermal protons gain $\sim 2\times$ more energy than nonthermal electrons. The acceleration processes include an injection followed by a prolonged Fermi acceleration phase. While the injection sets low-energy bounds of the power laws that control the nonthermal energy contents, the high-energy cutoffs keep growing with system size, indicating that the results can be extended to macroscopic systems.

Numerical simulations.—We use the vector particle-in-cell code that solves the Vlasov-Maxwell equations [20]. The 3D simulations start from a force-free layer $\mathbf{B} = B_0 \tanh(z/\lambda)\mathbf{e}_x + \sqrt{B_0^2 \mathrm{sech}^2(z/\lambda) + B_g^2}\,\mathbf{e}_y$ with a uniform plasma density $n_i = n_e = n_0$. B_0 is the reconnecting field, B_g is the guide field, and λ is the half-thickness of the layer, which is set to be one ion inertial length d_i. Electrons carry the initial current that satisfies Ampère's law. Most simulations have proton-to-electron mass ratio

$m_i/m_e = 25$, $b_g = B_g/B_0 = 0.2$, and $V_A = B_0/\sqrt{4\pi n_0 m_i} = 0.2c$, where c is the speed of light. The initial temperature $T_i = T_e = 0.01 m_i V_A^2$ so the plasma β based on the reconnecting field $\beta = 0.02$. The grid size is $\Delta x = \Delta y = \Delta z = 0.0488 d_i$, with 150 particles per cell per species. Boundary conditions are periodic in x and y, and conducting for fields and reflecting for particles in z. A small long-wavelength perturbation is included to initiate reconnection. To limit the influence of periodic boundaries, all simulations terminate around 1.3 Alfvén crossing time L_x/V_A before the acceleration stagnates. During this time, $\sim 1/3$ of the upstream flux is reconnected and thus the influence of the z boundary condition is minimal. Our simulations are important for multi-$\mathcal{X}$-line collisionless reconnection and also relevant for a hierarchy of collisional plasmoids that may develop kinetic-scale current layers to trigger collisionless reconnection [21–24]. A set of simulations have been conducted to confirm the robustness of the underlying processes for different guide fields β, domain sizes, and mass ratios. See Supplemental Material for a summary [25].

Kink instability and threshold for 3D effects.—Figure 1(a) shows the current density of flux ropes at $\Omega_{ci} t = 100$ in a simulation with $L_x \times L_y \times L_z = 150 \times 12.5 \times 62.5 d_i^3$ [26]. The flux ropes undergo $m = 1$ kink instability and its nonlinear evolution tears up the flux surfaces (also see the video in the Supplemental Material [25]). For comparison, flux ropes in the simulation with $L_y = 6.25 d_i$ (same L_x and L_z) do not have such dynamics [Fig. 1(b) [27]], although high-harmonic kink modes may develop. Figures 1(c) and 1(d) show the y-averaged energetic electron density ($1.2 < \varepsilon/m_i V_A^2 < 2.4$) of these two simulations, overplotted with Poincaré-type plots of magnetic field lines. Figure 1(c) shows that the kink

instability drives strong field-line chaos mixing up different flux surfaces while Fig. 1(d), in contrast, is nearly laminar.

The transition into the strong field-line chaos occurs when L_y reached a threshold L_{th}, controlled by the criterion of $m = 1$ kink disruption, namely, the safety factor at the edge of flux ropes $q_c = \pi b_g D/L_{th} \sim 1$ [28], where D is the flux-rope diameter. Closer examination finds $D \sim 15 d_i$ and $L_{th} \sim 9.5 d_i$, placing the $L_y = 12.5 d_i$ case above the threshold and the other one below it, consistent with the observed dynamics. This is in contrast to the earlier considered overlapping oblique tearing modes in the strong-guide-field regime [15–17]. In the Supplemental Material [25], we systematically verified this threshold and field-line chaos driven by the kink instability in the low-guide-field regime ($b_g < 0.5$).

The field-line chaos leads to particle transport out of flux ropes and further acceleration in the reconnection layer. Figure 1(c) also shows energetic electrons spreading out of flux ropes, whereas in Fig. 1(d) the electrons are effectively trapped in flux ropes. The chaotic fields can be further understood by field-line separations, namely, the distances between field-line pairs with small initial displacements [29,30]. Figure 2(a) shows the averaged separation of 10^3 field-line pairs, starting from the center of flux ropes with $D \sim 15 d_i$ [e.g., $x \sim 58 d_i$ in Fig. 1(c) and $x \sim 73 d_i$ in Fig. 1(d)] for several simulations with different L_y (the same L_x and L_z as Fig. 1). Above-threshold cases are far more chaotic (faster separation) than below-threshold cases. To better quantify particle transport, we also trace test-particle electrons with an isotropic initial velocity $V \sim 3.5 V_A$ from centers of the flux ropes [Fig. 2(b)]. Above-threshold cases consistently show stronger transport leaving the center of flux ropes. To understand the transport
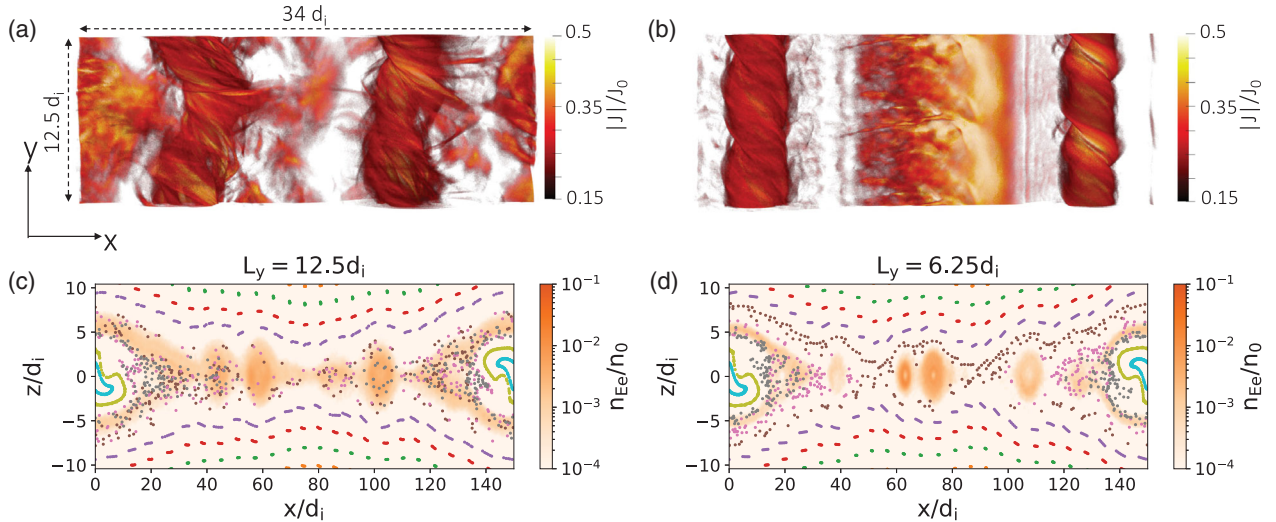

FIG. 1. Current density for simulations with $L_x = 150 d_i$ and different y dimensions (a) $L_y = 12.5 d_i$ and (b) $L_y = 6.25 d_i$, respectively. (c),(d) The y-averaged energetic electron density in these two simulations, respectively, overplotted with Poincaré-type plots of magnetic field lines—traced from $x = 0$ with their locations in the x–z plane recorded every $6.25 d_i$ in y and with different colors for different starting points.
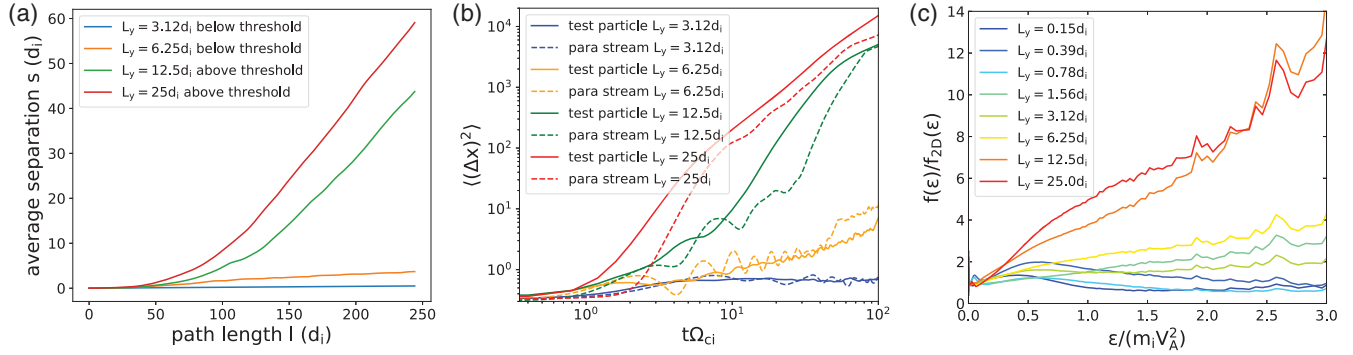
FIG. 2. (a) The averaged separation of initially adjacent field lines in the x–z plane traced from the center of flux ropes with $D \sim 15d_i$. (b) The mean-square displacement in x for test-particle electrons and parallel-streaming particles traced from the cores of the flux ropes. Test-particle electrons are injected with an initial isotropic velocity $\sim 3.5V_A$, while the parallel-streaming particles have a parallel velocity equal to the test-particles' root-mean-square parallel velocity. (c) The enhancement of energetic electrons in 3D compared with a 2D simulation.

mechanism, we calculate the displacement assuming particles just stream along field lines with a parallel speed $V_\parallel = 2V_A$ (root-mean-square value of the test-particle parallel velocities), which shows a trend similar to the test particles [Fig. 2(b)]. This suggests that streaming along the chaotic field lines is an important mechanism for particles to transport out of flux ropes. Particle transport enabled by flux-rope kink instability greatly enhances the efficiency of particle acceleration [Fig. 2(c)]. Above-threshold cases consistently produce about ~10 times more energetic particles (at energies ~100 times of the initial thermal energy) than the 2D case, whereas below-threshold cases only show moderate increase.

Simultaneous nonthermal acceleration of protons and electrons.—For larger reconnection domains, $L_{th} \sim \pi b_g D \sim 0.1\pi b_g L_x$ as D grows with L_x, verified by simulations with different sizes. Our 3D simulations exploiting this condition extend to an unprecedented reconnection domain $(L_x \times L_y \times L_z = 300 \times 25 \times 125d_i^3)$. We discuss nonthermal acceleration revealed by this simulation.

Figures 3(a) and 3(b) show time evolution of energy spectra over the whole domain for electrons and protons, with insets showing the corresponding spectral indices. Both electrons and protons evolve into clear power laws. While a smaller simulation ($L_x = 150d_i$) shows variable indices, the largest simulation shows that both electrons and protons sustain steady indices. Interestingly, protons took longer to settle into a steady power law ($\Omega_{ci}t \sim 225$), which has been challenging to achieve in previous simulations. Because of our simulation parameters, high-energy electrons become mildly relativistic, making their spectra softer [31,32]. More analysis shows protons and electrons have the same spectral index in momentum spectra [33]. The low-energy bounds of the power laws are nearly constant $\varepsilon_{le} \sim 0.2m_iV_A^2$ (electron) and $\varepsilon_{li} \sim 0.5m_iV_A^2$ (proton) over time. Meanwhile, the high-energy cutoffs persistently increase with longer time and larger domains [Fig. 3(c)],

reaching ~500 times of the initial thermal energy. This suggests the nonthermal spectra can extend to much higher energies in macroscopic systems.

The first-ever proton and electron power laws in kinetic simulations reveal the properties of the nonthermal components in magnetic reconnection. We determine the reconnected population by subtracting the cold upstream thermal distribution from the whole distribution. Out of this population, ~20% of particles and ~50% of energy for each species are nonthermal above the low-energy bounds. This efficiency is consistent with observations during solar flare reconnection [14,34–36]. Energetic protons gain about twice as much energy as electrons, likely due to a more efficient injection process, as we will discuss later.

In contrast, the spectra for below-threshold cases do not form clear and sustainable power laws for either species. Therefore, $L_y > L_{th}$ also serves as a condition for power-law formation. We have verified the dependence of L_{th} on guide fields using simulations with $b_g < 0.5$ and that the electron and proton spectra are insensitive to mass ratios in the range 25–100.

Particle acceleration processes.—Figure 3(d) shows the energy evolution of different generations of ions and electrons. Particles are selected if their final energies are above the corresponding low-energy bound and are averaged as one "generation" if the starting time of energization is within a $\Omega_{ci}\Delta t = 5$ interval. The energy evolution of each generation suggests that the accelerated particles experience an injection process followed by a prolonged Fermi acceleration phase, analogous to the two-stage acceleration process in relativistic turbulence [37,38]. The low-energy bounds of the power laws are determined by the injection energy. When cold protons first cross a reconnection exhaust, they receive an initial kick from the outflow ($V_{out} \sim 0.5V_A$ in our simulations, due to low b_g [39,40]) and gain a speed of about $2V_{out}$ (with $\varepsilon \sim \varepsilon_{li}$), which boosts their energy for further acceleration. Thus, at early time (e.g., $\Omega_{ci}t = 75$), most protons are bounded by
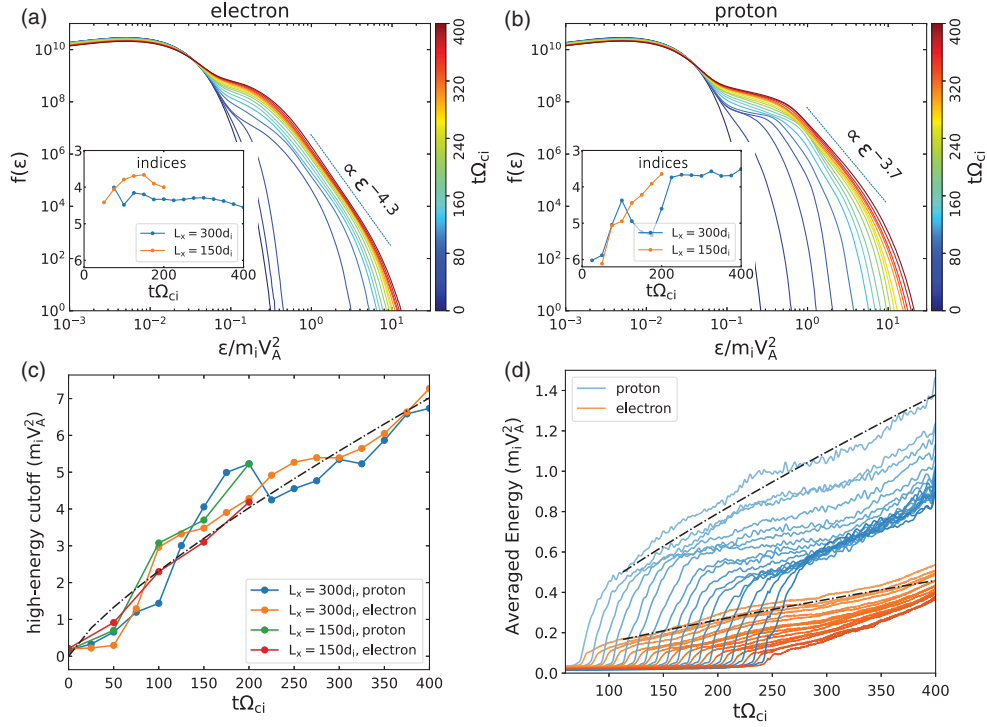
FIG. 3. Evolution of energy spectra for (a) electrons and (b) protons in the $L_x = 300d_i$ simulation. The spectral indices of this and a $L_x = 150d_i$ simulation are shown in the insets. (c) The high-energy cutoff of the power laws, determined by the energy at which the spectrum deviates from the fitted power law by 50%. (d) The energization history of different generations of injected particles. The dash-dotted lines represent the $\varepsilon \propto t^{0.8}$ scaling in (c) and (d).

ε_{li} in Fig. 3(b), and later acceleration shapes the distribution into a power law extending to higher energy. We have confirmed $\varepsilon_{li} \sim 0.5 m_i V_A^2$ with different simulations of low-β ($\lesssim 0.1$). On the other hand, electrons are much lighter, resulting in a less efficient energization process in the exhaust, where parallel electric fields could be important [10,37,41–46]. As a result, the electrons' low-energy bound $\varepsilon_{le} \sim 4 T_{\text{ex}}$, where T_{ex} is the electron temperature at the exhaust ($\sim 0.05 m_i V_A^2$ in this simulation). Note that T_{ex} can depend on many parameters (β, B_g, etc.), which will be studied in the future.

The Fermi acceleration process can be elucidated by the following scaling analysis. Since the Fermi acceleration rate at typical acceleration regions (exhausts) $\alpha \equiv \dot{\varepsilon}/\varepsilon \sim \mathbf{U}_E \cdot \boldsymbol{\kappa} \sim V_{Ax} \kappa_x$ and the escape rate from the reconnection layer $\tau_{\text{esc}}^{-1} \sim V_{Ax}/L$, the power-law index [47,48]

$$p = 1 + (\alpha \tau_{\text{esc}})^{-1} \sim 1 + \frac{V_{Ax}/L}{V_{Ax} \kappa_x} = 1 + \frac{1}{L \kappa_x}, \quad (1)$$

where $\mathbf{U}_E$ is the $E \times B$ drift speed, $\boldsymbol{\kappa}$ is the magnetic field curvature vector, and L is the half length of the recon-necting current sheet. Using $\kappa_x = (\hat{b} \cdot \nabla \hat{b})_x \sim \hat{b}_z \partial_z \hat{b}_x \sim B_z B_x/(B^2 \Delta_z)$, where Δ_z is the typical length scale of exhaust field lines in z (related to the scale of flux ropes), we obtain

$$p \sim 1 + \frac{B_x}{B_z} \frac{\Delta_z}{L} \left(1 + \frac{B_g^2}{B_x^2} \right). \quad (2)$$

$$\alpha \sim V_{Ax} \kappa_x = \frac{B_z V_{Ax} B_x^2}{B_x (B_x^2 + B_g^2) \Delta_z}. \quad (3)$$

Since both Δ_z and L are proportional to the domain size, in larger simulations the predicted spectral indices remain the same. In the acceleration regions (exhausts), taking $B_g^2/B_x^2 \ll 1$, $B_z \sim 0.05 B_x$, and $\Delta_z/L \sim 0.15$ typical during our simulations, we obtain $p \sim 4$, which is comparable to indices in our simulations. Since flux ropes grow over time, Δ_z increases (approximately linearly) and leads to a decrease in the acceleration rate $\alpha \sim C/t$, where C is a constant. More careful inspection to the time evolution of Δ_z suggests $C \sim 0.8$ (not shown). We also measure the acceleration rates directly from simulations as in Li *et al.* [13], finding values and dependence on time and simulation size consistent with the theoretical prediction. From the acceleration rate above, we obtain particle energy $\varepsilon \propto t^{0.8}$. This scaling agrees reasonably well with the growth of high-energy cutoffs [Fig. 3(c)] and particle energy evolu-tion [Fig. 3(d)] in the simulation. These demonstrate that both species are accelerated by Fermi acceleration into power laws, consistent with the highly correlated ion and electron acceleration observed in solar flares [5].

Discussion.—While observations have suggested efficient acceleration of both electrons and ions during nonrelativistic reconnection in solar flares and the magnetotail, establishing this from first-principle kinetic simulations has been a long-standing challenge. For the first time, our simulations produce power-law distributions for both electrons and protons that contain a significant amount of released energy, providing a plausible explanation to the solar flare observations [2–4,34–36]. The $p \sim 4$ spectra obtained in our simulations are consistent with the electron indices inferred from many x-ray and microwave observations [4,49], as well as the proton indices from gamma-ray [3] and solar-energetic-particle observations [50]. For the September 10, 2017 event observed by numerous instruments, comparison between magnetohydrodynamics simulations and gyrosynchrotron emission suggests reconnection occurred with a weak guide field ($b_g \sim 0.3$) [51]. Evidence of turbulent reconnection has been presented [52,53] for this event and the power-law index obtained by gyrosynchrotron emission is $p \sim 3.5$–6.5, broadly consistent with our simulations. Our simulations can also be compared positively with a well-observed magnetotail event reported by the Magnetospheric Multiscale Mission [6,7]. The event shows simultaneous electron and proton nonthermal acceleration in a broad turbulent reconnection region over ~ 16 Earth radii ($\sim 80 d_i$) with a low upstream β ($\beta_e \sim 0.03$), quite similar to our simulations. The observed power-law indices are typically ~ 3.3–4.3 for protons and ~ 4.2–5.4 for electrons, in agreement with our simulations. The shoulders of the observed spectra are ~ 15 keV ($0.2 m_i V_A^2$) for electrons and ~ 40 keV ($0.6 m_i V_A^2$) for protons, also similar to our simulations. Moreover, protons are observed to gain more energy than electrons.

We have demonstrated that flux-rope kink instability drives strong field-line chaos in 3D reconnection with weak guide fields, leading to strong particle transport and acceleration. As a result, both electrons and protons are accelerated into clear power laws, for which the basic properties such as efficiency and spectral indices are controlled by the injection and Fermi acceleration processes. The formation of the power laws, especially protons, requires large domain size in the reconnection plane and long acceleration time, as well as sufficient 3D physics to capture the flux-rope $m = 1$ kink instability. This work uncovers the fundamental processes for initializing and developing nonthermal ion and electron acceleration in nonrelativistic magnetic reconnection, with strong implications to not only heliophysics but also astrophysics, such as stellar flares and accretion-disk flares [54,55].

---

*qlzhanggo@gmail.com

[1] M. Yamada, R. Kulsrud, and H. Ji, Magnetic reconnection, Rev. Mod. Phys. **82**, 603 (2010).

[2] R. P. Lin, Energy release and particle acceleration in flares: Summary and future prospects, Space Sci. Rev. **159**, 421 (2011).

[3] N. Omodei, M. Pesce-Rollins, F. Longo, A. Allafort, and S. Krucker, Fermi-LAT observations of the 2017 September 10 solar flare, Astrophys. J. **865**, L7 (2018).

[4] D. E. Gary, B. Chen, B. R. Dennis, G. D. Fleishman, G. J. Hurford, S. Krucker, J. M. McTiernan, G. M. Nita, A. Y. Shih, S. M. White, and S. Yu, Microwave and hard x-ray observations of the 2017 September 10 solar limb flare, Astrophys. J. **863**, 83 (2018).

[5] A. Y. Shih, R. P. Lin, and D. M. Smith, RHESSI observations of the proportional acceleration of relativistic > 0.3 MeV electrons and > 30 MeV protons in solar flares, Astrophys. J. Lett. **698**, L152 (2009).

[6] R. E. Ergun et al., Magnetic reconnection, turbulence, and particle acceleration: Observations in the Earth's magnetotail, Geophys. Res. Lett. **45**, 3338 (2018).

[7] R. E. Ergun et al., Observations of particle acceleration in magnetic reconnection-driven turbulence, Astrophys. J. **898**, 154 (2020).

[8] J. F. Drake, M. Swisdak, H. Che, and M. A. Shay, Electron acceleration from contracting magnetic islands during reconnection, Nature (London) **443**, 553 (2006).

[9] J. T. Dahlin, J. F. Drake, and M. Swisdak, The mechanisms of electron heating and acceleration during magnetic reconnection, Phys. Plasmas **21**, 092304 (2014).

[10] J. T. Dahlin, J. F. Drake, and M. Swisdak, The role of three-dimensional transport in driving enhanced electron acceleration during magnetic reconnection, Phys. Plasmas **24**, 092110 (2017).

[11] X. Li, F. Guo, H. Li, and G. Li, Particle acceleration during magnetic reconnection in a low-beta plasma, Astrophys. J. 843, 21 (2017).

[12] X. Li, F. Guo, H. Li, and J. Birn, The roles of fluid compression and shear in electron energization during magnetic reconnection, Astrophys. J. 855, 80 (2018).

[13] X. Li, F. Guo, H. Li, A. Stanier, and P. Kilian, Formation of power-law electron energy spectra in three-dimensional low-β magnetic reconnection, Astrophys. J. 884, 118 (2019).

[14] H. Arnold, J. F. Drake, M. Swisdak, F. Guo, J. T. Dahlin, B. Chen, G. Fleishman, L. Glesener, E. Kontar, T. Phan, and C. Shen, Electron Acceleration during Macroscale Magnetic Reconnection, Phys. Rev. Lett. 126, 135101 (2021).

[15] K. Bowers and H. Li, Spectral Energy Transfer and Dissipation of Magnetic Energy from Fluid to Kinetic Scales, Phys. Rev. Lett. 98, 035002 (2007).

[16] W. Daughton, V. Roytershteyn, H. Karimabadi, L. Yin, B. J. Albright, B. Bergen, and K. J. Bowers, Role of electron physics in the development of turbulent magnetic reconnection in collisionless plasmas, Nat. Phys. 7, 539 (2011).

[17] Y.-H. Liu, W. Daughton, H. Karimabadi, H. Li, and V. Roytershteyn, Bifurcated Structure of the Electron Diffusion Region in Three-Dimensional Magnetic Reconnection, Phys. Rev. Lett. 110, 265004 (2013).

[18] M. Onofri, H. Isliker, and L. Vlahos, Stochastic Acceleration in Turbulent Electric Fields Generated by 3D Reconnection, Phys. Rev. Lett. 96, 151102 (2006).

[19] J. T. Dahlin, J. F. Drake, and M. Swisdak, Electron acceleration in three-dimensional magnetic reconnection with a guide field, Phys. Plasmas 22, 100704 (2015).

[20] K. J. Bowers, B. J. Albright, L. Yin, B. Bergen, and T. J. T. Kwan, Ultrahigh performance three-dimensional electromagnetic relativistic kinetic plasma simulation, Phys. Plasmas 15, 055703 (2008).

[21] K. Shibata and S. Tanuma, Plasmoid-induced-reconnection and fractal reconnection, Earth Planets Space 53, 473 (2001).

[22] L. Comisso, M. Lingam, Y. M. Huang, and A. Bhattacharjee, Plasmoid instability in forming current sheets, Astrophys. J. 850, 142 (2017).

[23] W. Daughton, V. Roytershteyn, B. J. Albright, H. Karimabadi, L. Yin, and K. J. Bowers, Transition from Collisional to Kinetic Regimes in Large-Scale Reconnection Layers, Phys. Rev. Lett. 103, 065004 (2009).

[24] H. Ji and W. Daughton, Phase diagram for magnetic reconnection in heliophysical, astrophysical, and laboratory plasmas, Phys. Plasmas 18, 111207 (2011).

[25] See Supplemental Material at http://link.aps.org/supplemental/10.1103/PhysRevLett.127.185101 for a summary of simulations and a video.

[26] The rendering has used a lower limit of $|J|$ to filter the upstream contents and emphasize the central regions of flux ropes to better visualize their motions.

[27] The domain in Fig. 1(b) has been replicated in y as it is periodic, to better compare with Fig. 1(a).

[28] E. Oz, C. E. Myers, M. Yamada, H. Ji, R. M. Kulsrud, and J. Xie, Experimental verification of the Kruskal-Shafranov stability limit in line-tied partial-toroidal plasmas, Phys. Plasmas 18, 102107 (2011).

[29] L. Yang, H. Li, F. Guo, X. Li, S. Li, J. He, L. Zhang, and X. Feng, Fast magnetic reconnection with turbulence in high Lundquist number limit, Astrophys. J. Lett. 901, L22 (2020).

[30] F. Guo, X. Li, W. Daughton, H. Li, P. Kilian, Y.-H. Liu, Q. Zhang, and H. Zhang, Magnetic energy release, plasma dynamics and particle acceleration during relativistic turbulent magnetic reconnection, Astrophys. J. 919 111 (2021).

[31] D. Caprioli and A. Spitkovsky, Simulations of ion acceleration at non-relativistic shocks. I. Acceleration efficiency, Astrophys. J. 783, 91 (2014).

[32] C. C. Haggerty and D. Caprioli, dHybridR: A hybrid particle-in-cell code including relativistic ion dynamics, Astrophys. J. 887, 165 (2019).

[33] F. Guo, X. Li, H. Li, W. Daughton, B. Zhang, N. Lloyd-Ronning, Y.-H. Liu, H. Zhang, and W. Deng, Efficient production of high-energy nonthermal particles during magnetic reconnection in a magnetically dominated ion-electron plasma, Astrophys. J. Lett. 818, L9 (2016).

[34] S. Krucker, H. S. Hudson, L. Glesener, S. M. White, S. Masuda, J. P. Wuelser, and R. P. Lin, Measurements of the coronal acceleration region of a solar flare, Astrophys. J. 714, 1108 (2010).

[35] M. Oka, S. Krucker, H. S. Hudson, and P. Saint-Hilaire, Electron energy partition in the above-the-looptop solar hard x-ray sources, Astrophys. J. 799, 129 (2015).

[36] M. J. Aschwanden, G. Holman, A. O'Flannagain, A. Caspi, J. M. McTiernan, and E. P. Kontar, Global energetics of solar flares. III. Nonthermal energies, Astrophys. J. 832, 27 (2016).

[37] L. Comisso and L. Sironi, Particle Acceleration in Relativistic Plasma Turbulence, Phys. Rev. Lett. 121, 255101 (2018).

[38] L. Comisso and L. Sironi, The interplay of magnetically dominated turbulence and magnetic reconnection in producing nonthermal particles, Astrophys. J. 886, 122 (2019).

[39] C. C. Haggerty, M. A. Shay, A. Chasapis, T. D. Phan, J. F. Drake, K. Malakit, P. A. Cassak, and R. Kieokaew, The reduction of magnetic reconnection outflow jets to sub-Alfvénic speeds, Phys. Plasmas 25, 102120 (2018).

[40] X. Li and Y.-H. Liu, The effect of thermal pressure on collisionless magnetic reconnection rate, Astrophys. J. 912, 152 (2021).

[41] T. D. Phan, M. A. Shay, J. T. Gosling, M. Fujimoto, J. F. Drake, G. Paschmann, M. Øieroset, J. P. Eastwood, and V. Angelopoulos, Electron bulk heating in magnetic reconnection at Earth's magnetopause: Dependence on the inflow Alfvén speed and magnetic shear, Geophys. Res. Lett. 40, 4475 (2013).

[42] M. A. Shay, C. C. Haggerty, T. D. Phan, J. F. Drake, P. A. Cassak, P. Wu, M. Øieroset, M. Swisdak, and K. Malakit, Electron heating during magnetic reconnection: A simulation scaling study, Phys. Plasmas 21, 122902 (2014).

[43] Q. Zhang, J. F. Drake, and M. Swisdak, Particle heating and energy partition in low-β guide field reconnection with kinetic Riemann simulations, Phys. Plasmas 26, 072115 (2019).

[44] Q. Zhang, J. F. Drake, and M. Swisdak, Instabilities and turbulence in low-β guide field reconnection exhausts with

kinetic Riemann simulations, Phys. Plasmas **26,** 102115 (2019).

[45] A. Le, J. Egedal, W. Daughton, W. Fox, and N. Katz, Equations of State for Collisionless Guide-Field Reconnection, Phys. Rev. Lett. **102,** 085001 (2009).

[46] C. C. Haggerty, M. A. Shay, J. F. Drake, T. D. Phan, and C. T. McHugh, The competition of electron and ion heating during magnetic reconnection, Geophys. Res. Lett. **42,** 9657 (2015).

[47] L. O. Drury, P. Duffy, D. Eichler, and A. Mastichiadis, On "box" models of shock acceleration and electron synchrotron spectra, Astron. Astrophys. **347,** 370 (1999), https://ui .adsabs.harvard.edu/abs/1999A%26A...347..370D/abstract.

[48] F. Guo, H. Li, W. Daughton, and Y.-H. Liu, Formation of Hard Power Laws in the Energetic Particle Spectra Resulting from Relativistic Magnetic Reconnection, Phys. Rev. Lett. **113,** 155005 (2014).

[49] M. Oka, J. Birn, M. Battaglia, C. C. Chaston, S. M. Hatch, G. Livadiotis, S. Imada, Y. Miyoshi, M. Kuhar, F. Effenberger, E. Eriksson, Y. V. Khotyaintsev, and A. Retinò, Electron power-law spectra in solar and space plasmas, Space Sci. Rev. **214,** 82 (2018).

[50] C. M. S. Cohen *et al.*, Parker Solar Probe Observations of He/H Abundance Variations in SEP Events inside 0.5 AU, Astron. Astrophys. **650,** A23 (2020).

[51] B. Chen, C. Shen, D. E. Gary, K. K. Reeves, G. D. Fleishman, S. Yu, F. Guo, S. Krucker, J. Lin, G. M. Nita, and X. Kong, Measurement of magnetic field and relativistic electrons along a solar flare current sheet, Nat. Astron. **4,** 1140 (2020).

[52] X. Cheng, Y. Li, L. F. Wan, M. D. Ding, P. F. Chen, J. Zhang, and J. J. Liu, Observations of turbulent magnetic reconnection within a solar current sheet, Astrophys. J. **866,** 64 (2018).

[53] R. J. French, P. G. Judge, S. A. Matthews, and L. van Driel-Gesztelyi, Spectropolarimetric insight into plasma sheet dynamics of a solar flare, Astrophys. J. Lett. **887,** L34 (2019).

[54] B. Ripperda, F. Bacchini, and A. A. Philippov, Magnetic reconnection and hot spot formation in black hole accretion disks, Astrophys. J. **900,** 100 (2020).

[55] A. Nathanail, C. M. Fromm, O. Porth, H. Olivares, Z. Younsi, Y. Mizuno, and L. Rezzolla, Plasmoid formation in global GRMHD simulations and AGN flares, Mon. Not. R. Astron. Soc. **495,** 1549 (2020).